Extensive wind tunnel tests measurements of dynamic stall phenomenon for the OA209 airfoil including 3D effects

Arnaud Le Pape [1], Guy Pailhas [2], Frédéric David [3], Jean-Michel Deluc [4]

[1]Applied Aerodynamics Department
[2]Aerodynamics and Energetics Models Department
[3]Structural dynamics and coupled systems Department
[4] Fauga-Mauzac wind tunnels Department

ONERA, BP 72, 29 avenue de la Division Leclerc
92322 Châtillon, France

Key words: Dynamic Stall, OA209 airfoil, wind tunnel tests, LDV, PIV

Abstract: Wind tunnel tests of a OA209 airfoil under dynamic stall conditions have been conducted in the ONERA F2 wind tunnel. Three wind tunnel entries using three OA209 models (two 2D and one 3D) were performed. Among all the tests points measured, a limited number of dynamic stall configurations have been fully investigated using numerous measurement techniques in order to obtain unsteady pressure distributions and aerodynamic forces, unsteady skin frictions distributions and mean and turbulent flowfield. Flowfield measurements were obtained thanks to Laser Doppler Velocimetry (LDV) and Particle Image Velocimetry (PIV) techniques. Several features of dynamic stall have been studied during these tests such as Reynolds effects, dynamic stall onset and 3D effects. The experimental results are presented and discussed in the paper through these dynamic stall characteristics. Finally the dynamic stall results on the 3D finite-span wing are detailed, highlighting the interaction between the dynamic stall vortex and the tip vortex and the importance of the sweep effect.

INTRODUCTION

Among aerodynamic issues encountered on helicopter rotors, dynamic stall is one of the most challenging both considering the understanding of the physical phenomenon and considering the numerical simulation of the dynamic stall. This phenomenon appearing when the blade section angle of attack goes beyond the static stall angle, is one of the main limitations of helicopter advancing speed. Indeed, dynamic stall occurs mainly on the retreating blade side area at high advance ratios, conditions associated with large angles of attack and low incoming flow velocities. Under these incoming conditions, the flow over the blade section separates abruptly with the formation of a strong dynamic stall vortex that leads to a brief increase of the maximum lift that drops suddenly, and a very large negative pitching moment. The sudden and strong negative pitching motion induces large pitch-links loads and vibratory loads. From an aerodynamic point of view, the dynamic stall phenomenon is an unsteady, turbulent, compressible phenomenon; this very complex problem was studied by many authors using experimental and numerical works that highlighted the importance of various parameters: Reynolds number, Mach number, transition, leading-edge curvature, etc… Since the dynamic stall phenomenon remains very difficult to simulate, most of the findings were achieved thanks to experimental studies. Generally speaking, experiments [1-3] were conducted using pitching 2D models, which was shown to be representative of dynamic stall. All these wind tunnel tests provided a useful overview of dynamic stall features such as dynamic stall onset, sensitivity to Reynolds and Mach numbers, to airfoil geometry, and they also provided a few quantitative measurements on aerodynamic loadings. However, most of these experiments were often mainly focused either on wall measurements, or on flowfield measurements. Some of the published experiments investigated 3D effects, with a very few quantitative measurements [4-6].

In the continuation of all this experimental work, an ambitious wind tunnel tests program was launched at ONERA in order to obtain very detailed surface measurements (pressure distributions, skin friction) but also flowfield measurements (LDV, PIV) for a OA209 airfoil under dynamic stall conditions, including investigations of various parameters: Reynolds number influence, 3D effects, sweep effects, laminar-turbulent boundary layer transition. For that purpose 3 models of the OA209 airfoil were manufactured including a finite-span 3D wing model and 3 wind tunnel entries were performed. The tests conducted in the ONERA F2 wind tunnel are first briefly described. The various measurements performed during the 3 wind tunnel entries are then presented and the accuracy and repeatability of each measurement technique is shown. Experimental results are finally discussed from 3 points of view: the onset of dynamic stall, the influence of Reynolds number and the 3D effects induced by dynamic stall.

1. EXPERIMENTAL SET-UP

1.1 F2 subsonic wind-tunnel

The wind tunnel tests were conducted in the ONERA F2 wind-tunnel. This research facility has a test section of 1.4 meters wide, 1.8 meters high and 5 meters long; wind speeds up to 100 m/s can be reached. The wind-tunnel walls are made of glass panels that allow a full optical access to the test section and that make F2 wind tunnel particularly suitable for tests that requires a detailed flowfield investigation.

1.2 OA209 models

Three OA209 airfoil models were built for the F2 dynamic stall wind-tunnel tests: two 2D models with 2 different chord length (500mm and 300mm) and a span length equal to the test section width and one 3D model with a chord length equal to 300 mm and a span length equal to 900mm. All the models are made of two carbon skins stuck together and containing low density polyurethane material that ensures light models suitable for dynamic tests. The pitching oscillations are forced on one side by a driving mechanism that delivers sinusoidal oscillations of various amplitudes and frequencies. In addition the 3D model allows 3 sweep configurations: sweep angle equal to -30° (forward), 0°, +30° (backward).

The models were equipped with numerous transducers summarized in the table below, that allowed the detailed measurements described in section §2.

C500 (chord=500mm)	C300 (chord=300mm)	C300-3D (chord=300mm, span=900mm)
55 pressure taps 40 Kulites transducers 20 hot films on upper surface 9 skin friction gauges 2 accelerometers	54 pressure taps 40 Kulites transducers 20 hot films on upper surface 10 skin friction gauges 2 accelerometers	112 Kulites transducers 7 accelerometers 8 optic fibres

Table 1: OA209 models equipment

Figure 1: Dynamic stall OA209 models in F2 wind tunnel test section – Left: C500, middle: C300, right: C300-2D

As shown in Figure 1 most of the measurements are located at mid-span of the 2D models. For the 3D model, 4 spanwise locations were instrumented using Kulites transducers: r/R=0.5/0.8/0.95/0.99.

1.3 Tests programs overview

Numerous test points were performed during the three test campaigns allowing a deep investigation of the dynamic stall phenomenon. For each campaign the test program was conducted as following:

- static configuration for various angles of attack,
- parametric study of the pitching airfoil using a sinusoidal oscillation, variation of mean angle of attack, amplitude and reduced frequency,
- deep investigation of a limited number of dynamic stall configurations.

The outcome of each parametric study was thus the selection of the following dynamic stall cases for a reduced frequency set to k=0.1:

C500 (Re=1.8M)	C300 (Re=1M, 0.5M)	C300-3D (Re=1M, 0.5M)
1 Deep Stall case: α=13°+/-5° 1 Moderate Stall case: α=12°+/-5°	1 Deep Stall case: α=13°+/-5° (for the 2 Re numbers)	1 Deep Stall case: α=17°+/-5° (for 3 sweep angles: -30°, 0°, +30°)

Table 2: Selected dynamic stall cases for each wind tunnel test

2. MEASUREMENTS

The following table presents the available measurements for each case of the experimental database:

Cases		Aerodynamic coefficient	Kp	LDV	PIV	Friction
C500 - Re=1.8M	Deep Stall	x	x	x		x
	Moderate Stall	x	x	x		x
C300 - Re=1M	Deep Stall	x	x	x		x
C300 - Re=0.5M	Deep Stall	x	x	x		x
C300-3D - Re=1M	Deep Stall	x	x	x	x	
C300-3D - Re=0.5M	Deep Stall	x	x		x	

Table 3: Measurements performed for each dynamic stall case

Details on the different measurements performed are given in the next paragraphs.

2.1 Pressure distributions, aerodynamic coefficients

Static pressure distributions were measured using pressure taps distributed on the upper and lower surfaces of each model. The pressure taps are distributed over 4 spanwise locations, all the instrumentations couldn't indeed be located in the same section.
Unsteady pressure distributions are measured using Kulites transducers (+/-5 PSI range). For each test point several measurement blocks (between 5 and 300) were acquired triggered with the oscillating motion of the airfoil, each block corresponding to 2048 samples at a sampling rate of 2 kHz. This allowed to have a large number of pitching oscillations cycles measured (up to 900 cycles) and to compute an average value and a standard deviation for each measured quantity [7]. All the results are thus presented with error-bars that represent the [-σ ; +σ] interval, with σ the estimated standard deviation.
Lift and moment coefficients are then determined by pressure integration at each instant of the pitching oscillation cycle. The total drag was also measured thanks to wake measurements performed using LDV downstream the airfoil. However, such data are only available for the static cases.

2.2 LDV measurements

Mean flow velocities and turbulent quantities were measured on the suction side of the airfoil using LDV (3D laser velocimetry). A detailed description of the LDV system installed in the F2 wind-tunnel is provided in [7], [8]. For the dynamic stall cases, the measurements were synchronized with the model pitching motion: for each measurement point 72000 samples were recorded, these samples are then sorted to 36 instants, each instant corresponding to 10 degrees of phase of the oscillating motion. Phase-averaged and rms values of the 3 components of the velocity were then computed. Using this methodology, an average of 2000 samples should be used for each point and for each instant of the oscillating cycle. However some seeding problems in the separated flow region lead to an unfair balance between the different measurement points and instants of the pitching motion. The LDV measurements methodology was thus improved all along the different tests campaigns. 40000 samples measurements were added in the separated region clustered during the phases when large dynamic stall separation occurs over a range equivalent to 100 degrees of phase. A comparison of acceptable samples number (blanking corresponds to the points for which the number of samples is insufficient to obtain converged average velocity values) for 2 diffirent wind tunnel campaign test points corresponding to a largely separated flows is presented in Figure 2, showing the improvement of the LDV measurements during these dynamic stall tests.

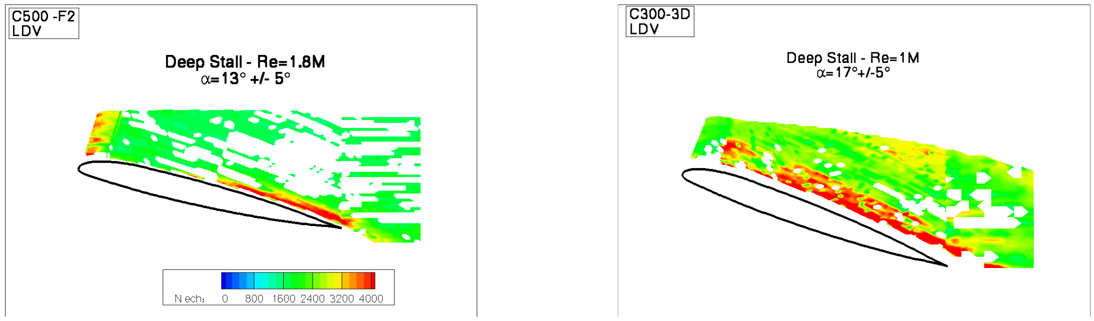

Figure 2: Comparison of LDV window showing the conserved accurate measurements (unsatisfactory data are blanked) for two wind tunnel tests

It was observed during all the tests that the samples number used for the phase averaging is a critical parameter. Non-reproducibility of such separated flows has been discussed by many authors as far as phase-averaging measurements are concerned [9-10]; in the presented results fluctuations in the separated flows have been successfully reduced thanks to a high number of measurements samples used for the averaging.

2.3 PIV measurements

2C and 3C PIV measurements were performed during these tests using a pulsed 2x240mJ laser source. Laser sheets were generated either parallel to the freestream direction as for LDV measurements or perpendicular to the freestream direction in order to investigate the cross-flow and the 3D effects due to the dynamic stall vortex. The flow was seeded downstream the test section using oil droplets. Each oscillating cycle of the airfoil was discretized in 26 instants. Each measurement at each instant is the result of a phase averaging over 200 pictures. Some PIV results are presented in the next paragraphs for the 3D model.

2.4 Skin friction measurements

For both 2D models, hot films and skin friction gauges were used to measure the instantaneous skin friction with respect to oscillating phase angle. The detailed description of the experimental procedure is given in [7] and the skin friction gauges calibration is fully described in [11]. Hot films were located between 5% and 35 % of the airfoil chord and allowed the absolute value of the skin friction to be determined. Skin friction gauges were located between 5% and 75% and allowed to get both the absolute value and the sign of the skin friction to be measured. Samples of results are presented in the next section.

3. EXPERIMENAL RESULTS

3.1 Overview of the results

During the three wind tunnel entries representing in total around 6 months of wind-tunnel occupancy, numerous test points were performed and for some specific test points listed in Table 2, very detailed measurements were performed. Figure 3 presents a comparison of static and dynamic aerodynamic coefficients measured during the C500 test campaign (Re=1.8 M). The top case is a deep stall case with a strong hysteresis effect and a large negative pitching moment. One can notice the increased maximum lift for the dynamic case in comparison to the static one. The second case is a moderate stall case that is obtained by lowering the mean angle of attack of the pitching airfoil; a smaller hysteresis loop and negative pitching moment are thus reached. This figure also highlights the post-processing work performed on each test point [pailhas] that allowed to provide error-bars for each measurement; error-bars representing the [-σ;+σ] with σ the standard deviation of the measured quantity.

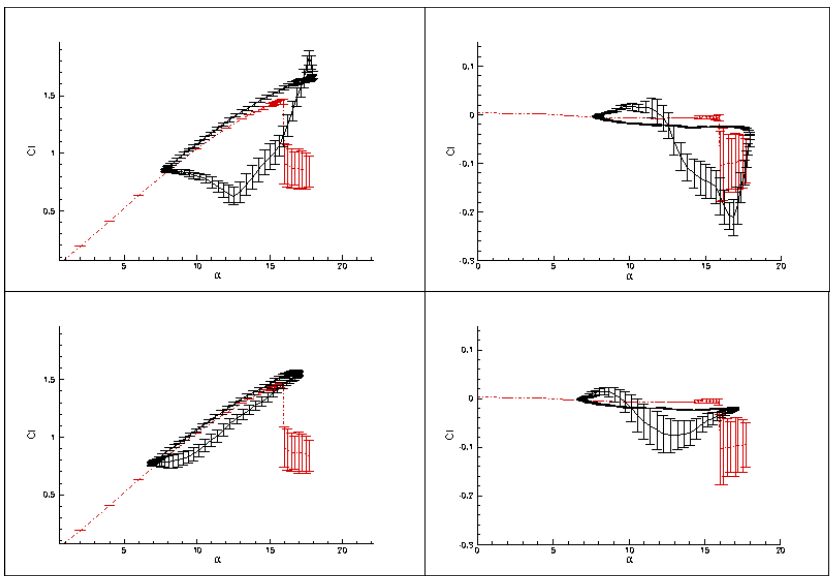

Figure 3: Comparison of static (red) and dynamic stall (black) cases on the C500 model at Re=1.8M

The next paragraphs present experimental results focusing on several specific features of the dynamic stall phenomenon providing a good overview of all measurements performed.

3.1 Dynamic stall onset

An important literature is available on the understanding of the dynamic stall phenomena and in particular on its onset. Indeed dynamic stall onset has been shown to be very sensitive to inflow conditions such as freestream Mach number, Reynolds number, reduced frequency of the pitching motion, local curvature of the leading-edge [12-13]. The main conclusions highlight that the dynamic stall vortex creation is linked to a strong adverse pressure gradient that leads in most cases to a laminar separation bubble. At low Mach number, much of the dynamic stall onset is driven by the laminar separation bubble that burst creating the dynamic stall vortex. For compressible flows, the shock induced separation is the major contributor to the dynamic stall onset [12].

In the present case, the tests were done with free laminar-turbulent transition of the OA209 airfoil which has an important leading-edge curvature. The tests were also conducted at low Mach number (M~0.16) for moderate Reynolds numbers. First static pressure data shows the presence of a laminar separation bubble at moderate angles of attack for Reynolds numbers between 0.4M and 1M; in Figure 4, the pressure plateau, characteristic of the laminar bubble can be clearly seen at the leading-edge on the suction side. At higher Reynolds numbers (Re=1.8M), the laminar bubble is more difficult to detect; the length and height of the laminar separation bubble have been shown to dramatically be lowered for increasing Reynolds numbers [14], and the bubble is expected to be shifted to the very leading-edge where an insufficient number of pressure taps are available to capture it. Numerical studies (LES computations) [15] showed the presence of a bubble at this Reynolds number.

The presence of a transitional laminar bubble was also confirmed at Re=1.8M for the OA209 airfoil under oscillating pitching motion thanks to hot-films measurements [7]; a leading-edge separation rapidly shed downstream was demonstrated. Similar conclusions can be drawn from lower Reynolds number tests. Figure 5 shows for example the skin friction gauges results depending on the oscillating motion at Re=0.5M. The separated area corresponds to negative skin frictions zone which clearly appear at the leading-edge and extend downstream the trailing edge.

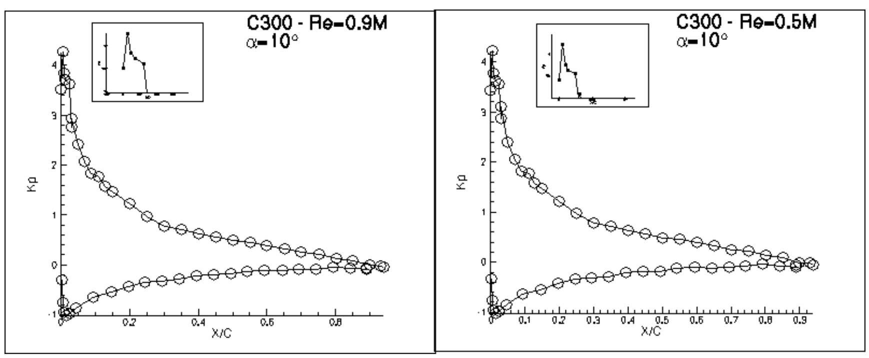

Figure 4: Static pressure distribution for two Re numbers showing the presence of a laminar bubble separation

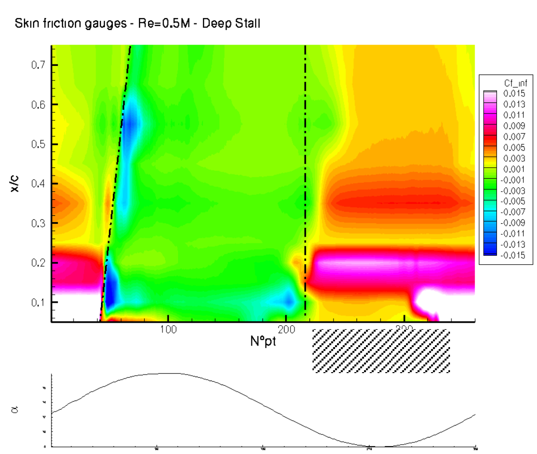

Figure 5: Skin friction measurements (gauges) with respect to oscillating angle of attack at Re=0.5M (dashed area corresponds to measurement problems)

The development and the shedding of the dynamic stall vortex downstream from the leading-edge of the airfoil is well illustrated for the different deep stall cases corresponding to various Reynolds numbers, thanks to LDV measurements. Figure 6 shows thus the streamwise velocity component at three instants around the stall occurrence for deep stall cases at Re=0.5M/1M/1.8M. The leading-edge separation is clearly visible, and one can notice how sudden this separation occurs. The separation is associated with a maximum of turbulent kinetic energy as shown in Figure 7. In particular the LDV measurements at Re=0.5M near the leading-edge of the airfoil presents just before stall an area of high turbulent kinetic energy at the airfoil surface that is very likely due to the laminar bubble separation bursting. Laminar bubble separation is indeed known to be associated with a peak of turbulent kinetic energy at the turbulent reattachment [15-16]

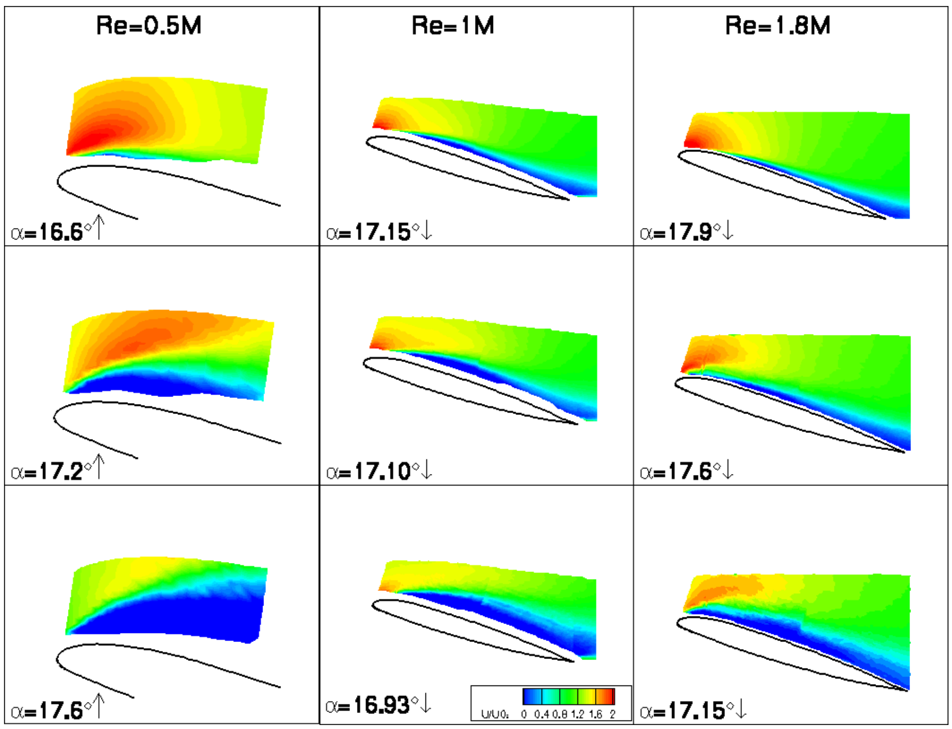

Figure 6: Streamwise velocity measured on the upper surface of the OA209 airfoil under deep stall conditions by LDV for different Reynolds numbers around stall angles of attack

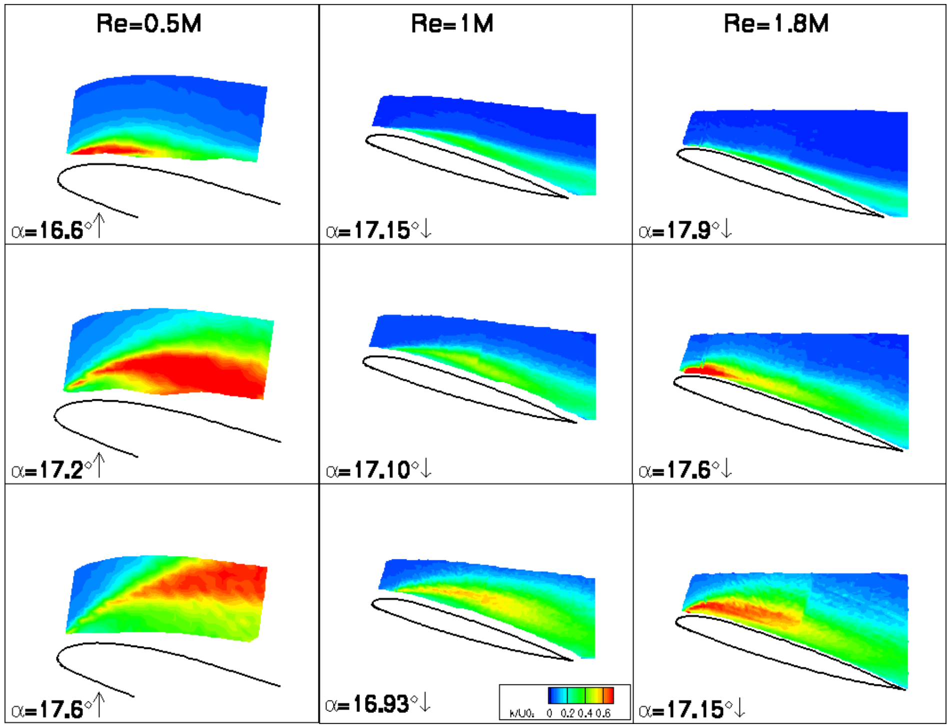

Figure 7: Turbulent kinetic energy measured on the supper surface of the OA209 airfoil under deep stall conditions by LDV for different Reynolds numbers around stall angles of attack

3.2 Reynolds number effect

One of the objectives of these wind tunnel tests was to obtain experimental dynamic stall data for different Reynolds numbers from 0.5 M to 1.8M, a range quite representative of Reynolds numbers encountered in actual flight conditions. Figure 8 presents the static lift curve for three Reynolds numbers, showing that the stall angle of attack is lowered from 16 degrees at Re=1.8M to 11.5 degrees at Re=0.5M.

Identical observations can be made about the Reynolds number effect for the dynamic stall cases presented in Figure 9. The larger the Reynolds number is, the later the leading-edge separation appears. The stall is thus stronger at low Reynolds number and the aerodynamic coefficients hysteresis loops are also stronger with decreasing Reynolds number. At Re=1M and Re=1.8M, the influence of the Reynolds number is not very important [17]. However, the Re=0.5M case is different from the others. A lift increase is observed before the maximum angle of attack, a low negative pitching moment is also simultaneously observed. Leading-edge separation seems to occur before the maximum angle of attack, which is confirmed by the LDV measurements presented in Figure 6 and Figure 7. At this low Reynolds number, the laminar bubble separation is expected to be larger and the laminar separation bubble bursting seems to appear earlier.

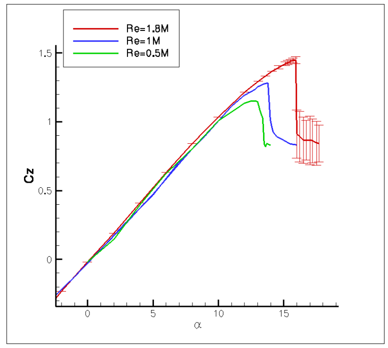

Figure 8: OA209 static polar for different Reynolds numbers

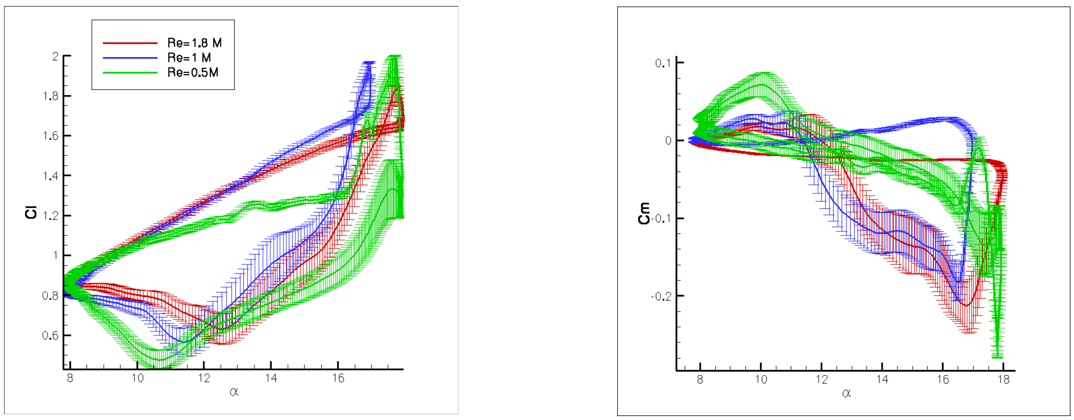

Figure 9: Deep stall lift and moment hysteresis loops for three different Reynolds numbers

3.3 3D flows on the 2D airfoil

During the main part of the oscillating pitching motion, LDV measurements showed that the flow is 2-dimensional with a transverse velocity component close to zero. But as mentioned in [7], a significant transverse velocity appears when the flow separates and the dynamic stall occurs. Figure 10 presents LDV measurements of the transverse velocity component for the three deep stall cases at different Reynolds numbers at stall. A 3D flow component appears in the separated area and in the shear layer; this transverse velocity component can reach up to 20% of the incoming freestream velocity. These experimental results highlight that, when stall occurs, an important 3D flow appears until the flow reattaches, even for a 2D model.

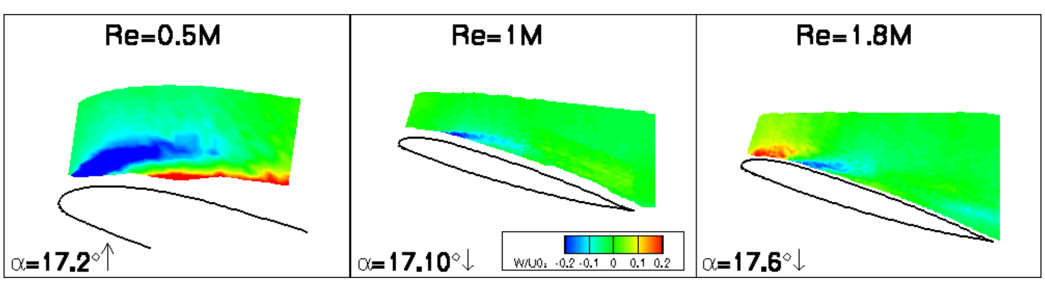

Figure 10: Transverse velocity component measured by LDV for three deep stall cases at stall for three Re numbers

3.4 3D finite span effects (sweep angle=0°)

The lift coefficient obtained from pressure integration is presented in Figure 11 for the static 3D finite span model at different spanwise locations in comparison with the static 2D lift coefficient. The expected reduction of the Cl(α) slope due to 3D effects is well observed. At mid span (red curve) a sharp stall identical to the one obtained with the 2D model is observed. This stall occurs at a higher angle of attack of 20 degrees due to the induced velocity field mainly created by the tip vortex. The lift stall is less and less sharp from the inner section to the wing tip. At the tip, the effect of the tip vortex can be clearly noticed with the non-linear Cl(α) slope.

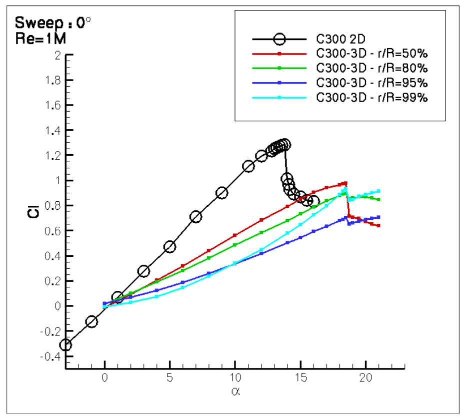

Figure 11: Lift coefficient for the static 3D finite span wing compared to 2D lift coefficient

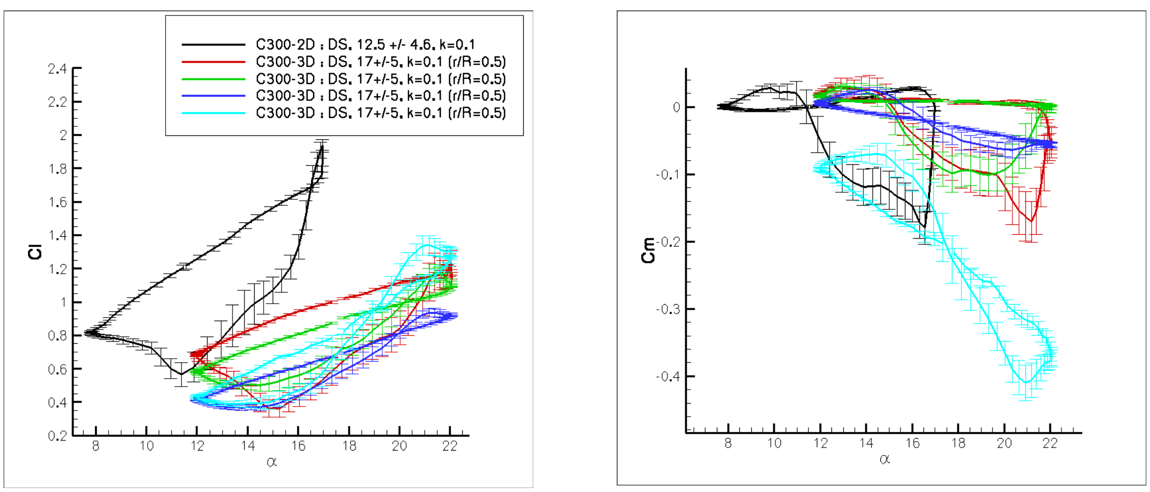

Figure 12: Comparison of lift and moment hysteresis curves for the 3D finite span wing and the 2D model-Re=1M

Figure 12 presents the lift and moment hysteresis curves for the selected deep stall cases for both the 3D and 2D models at a Reynolds number equal to 1M. The 3D deep stall case was chosen in order to have a similar pitching moment behavior in the section at mid span between the 3D and the 2D models. In order to achieve this objective, the mean angle of attack was increased from 12.5° to 17° (static stall angles are 14° and 20° respectively) keeping a similar amplitude and reduced frequency. If the dynamic stall characteristics are very comparable between the mid-span section results in 3D and 2D, on the 3D model the lift and moment hysteresis curves are very different near the wing tip. Once again the effect of the tip vortex is clearly visible leading to a weaker negative pitching moment and a more limited lift hysteresis near the blade tip. At the wing tip, lift and moment hysteresis are totally driven by the tip vortex.

The interaction between the dynamic stall vortex and the wing tip vortex can be investigated thanks to LDV and PIV measurements. Figure 13 presents a phase-averaged view of both PIV and LDV fields at a given instant during the nose down airfoil motion when the flow is fully separated. One can notice that the separation extents from the leading-edge to the trailing edge of the wing but not all along the span. The flow seems to remain attached at the blade tip.

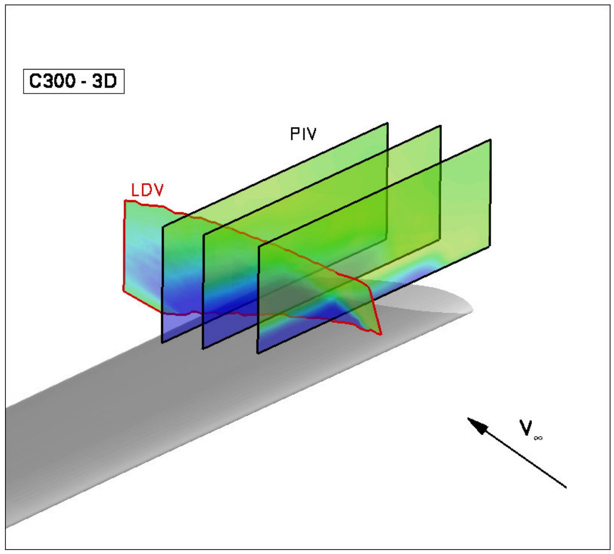

Figure 13: Example of LDV and PIV results on the 3D model

PIV measurements at mid-chord for different instants around stall are presented in Figure 14, where are plotted on the left side the streamwise velocity and streamlines in the PIV plane, and on the right side the vorticity magnitude. Before stall during the upstroke motion at α=17.2°, the flow is attached and the only feature of the flowfield to be noticed on the streamlines and the vorticity is the wing tip vortex. At a higher angle of attack, α=21.2°, the thickening of the boundary layer can be seen, the flow starts to separate and this separation seems to start from the inner part of the wing to the wing tip. At the maximum angle of attack α=22° the flow is totally separated, and the stall is clearly more pronounced on the inner part of the wing than at the tip. The tip vortex can still be seen on the PIV measurements and this tip vortex seems to block the dynamic stall at a spanwise location equivalent to r/R=0.85. This observation is confirmed at an angle of attack α=19.6° during the downstroke motion at which the flow is fully separated; the inner part of the wing is stalled but the flow remains attached at the blade tip due to the interaction between the dynamic stall vortex and the tip vortex. Indeed the wing tip vortex acts as a barrier against the dynamic stall vortex. The reattachment follows an inverse process: the flow reattachs from the wing tip to the inner part of the wing as shown by the PIV measurements at α=16.4°.

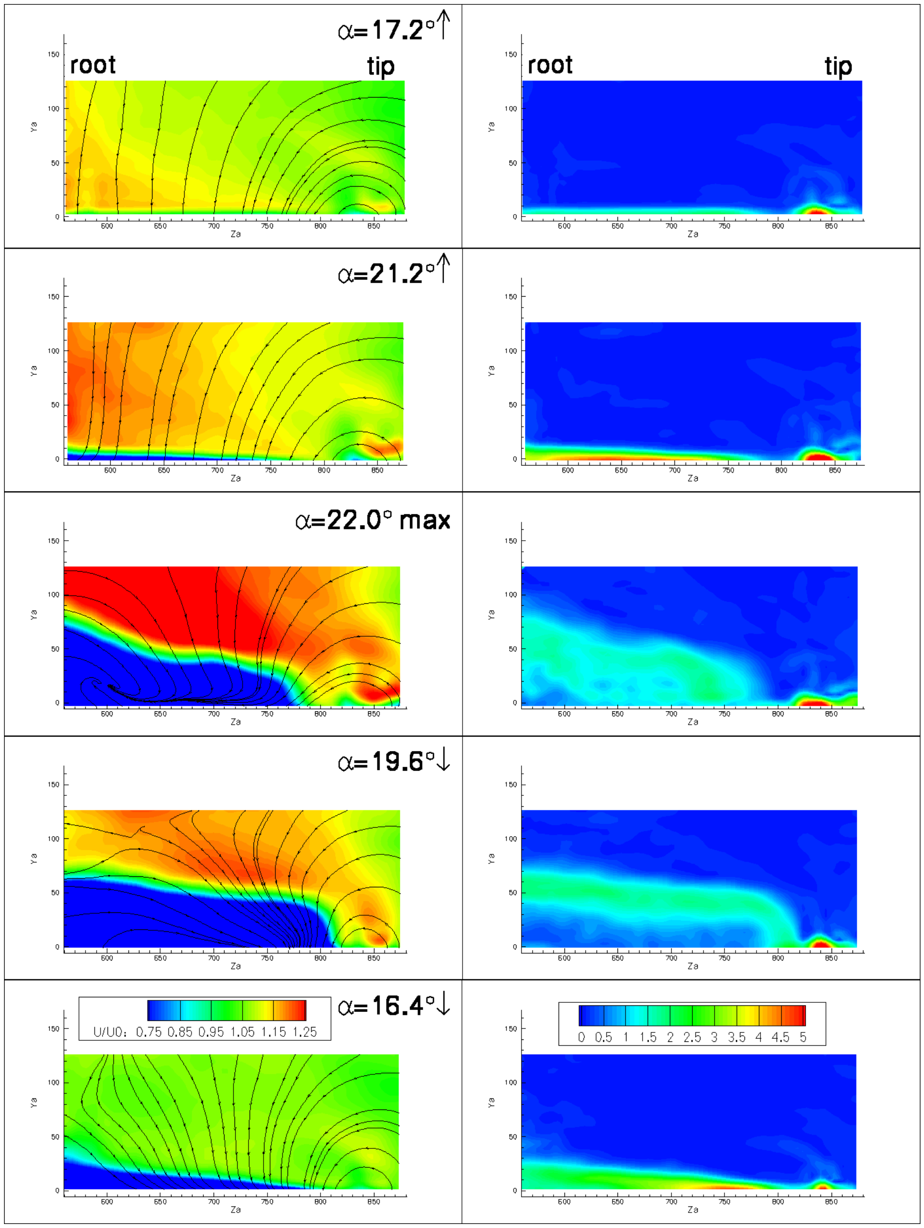

Figure 14: PIV results at x/c=50% on the 3D model – 4 phase-averaged measurements at 4 instants around stall – Streamwise velocity and streamlines (left), vorticity (right) – deep stall α=17°+/-5°, Re=1M

The interaction between the tip vortex an the dynamic stall vortex thus plays an important role, and this interaction strongly depends on the sweep angle of the wing. Indeed, depending on the wing sweep angle the tip vortex path will be different and the interaction with the dynamic stall will be modified. This is illustrated in Figure 15 with tuft visualization for two sweep angles and static stall conditions. For zero sweep angle, the flow separation is stopped by the wing tip vortex when the wing is fully stalled with a positive sweep angle, since the wing tip vortex is convected away from the wing suction side.

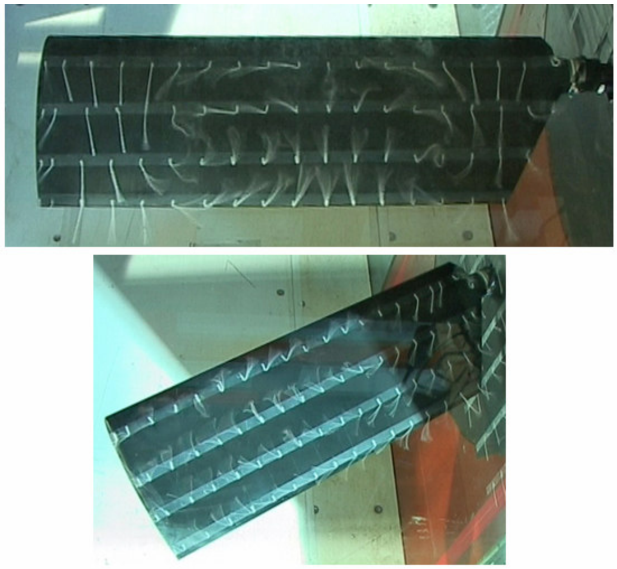

Figure 15: Tufts visualization on the C300-3D model for zero sweep angle (top) and 30° sweep angle (bottom) at stall

4. CONCLUSIONS

A large dynamic stall experimental study has been performed at ONERA for a OA209 airfoil, using 2D and 3D models. Numerous detailed wall and flowfield measurements were performed for a limited number of dynamic stall configurations providing a very complete experimental database for the dynamic stall phenomenon. The dynamic stall onset was first discussed, highlighting the importance of the laminar bubble separation at the leading-edge on the dynamic stall vortex creation for low incoming Mach numbers. Indeed a laminar bubble separation is detected for static cases for various Reynolds number and a typical laminar-turbulent transition due to a laminar separation bubble was also observed. The LDV measurements highlight in addition the leading-edge separation associated with a burst of kinetic turbulent energy. The dynamic stall onset since driven by the laminar separation bubble is sensitive to the Reynolds number and the experimental results show that the stall appears later with increasing Reynolds numbers. At low Reynolds number, the stall can even appear before the maximum angle of attack. Finally, the flowfield investigations on the 3D model thanks to LDV and PIV provided an insight on the interaction between the wing tip vortex and the dynamic stall vortex. Indeed the dynamic stall separation that spreads from the inner part of the wing to the tip is blocked by the wing tip vortex and the wing tip remains attached during the airfoil pitching motion. Swept effect is expected to have a major influence on this interaction as confirmed by the tufts visualization. However a large part of the experimental database remains to be analyzed, in particular the 3D data for the swept wing. The experimental database thus obtained on the dynamic stall is a useful tool for the validation of simulation codes and is expected to help the improvements of dynamic stall modeling.

ACKNOWLEDGMENT

The authors would like to thank all the people involved in the three wind tunnel test campaigns and who helped to obtain this very detailed experimental database on dynamic stall.

REFERENCES

[1] McCroskey W. J., Carr L. W., McAllister K. W., *Dynamic stall experiments on oscillating airfoils*, AIAA Journal, Vol.14, n°1, January 1976

[2] Dadone L., U., Two-*dimensional wind tunnel test of an oscillating rotor airfoil*, NASA CR-2914, December 1977

[3] Pizialli R. A., *2D and 3D oscillating wing aerodynamics for a range of angles of attack including stall*, NASA Technical M. 4632, USAATCOM Technical Report 94-A-011, September 1994

[4] Lorber P. F., Covino A. F., Carta F. O, "*Dynamic stall experiments on a swept three-dimensional wing in compressible flow*" , 22nd AIAA Fluid dynamics, Plasma dynamics and Lasers Conference, June 24-26, 1991, Honolulu, Hawai

[5] Yang H. Q., Przekwas A. J., "*Dynamic stall on a three-dimensional rectangular wing*", 31st Aerospace Sciences Meeting and Exhibit, January 11-14, 1993, Reno (NV), USA

[6] Szafruga J., Ramaprian B. R., "*LDA measurements in the three-dimensional flow over an oscillating rectangular wing*", AIAA-97-1935, 1997

[7] Pailhas G., Houdeville R., Barricau P., Le Pape A., Faubert A., Loiret P., David F., "*Experimental investigation of dynamic stall*", 31st European Rotorcraft Forum, 13-15 Sept, 2005, Florence, Italy

[8] Boutier A., Lfèver J., Micheli F., "*Analysis of helicopter blade vortex structure by laser velocimetry*", Experiments in Fluids, Vol. 21, 1996, pp33-42

[9] Raffel M, Kompenhans J., Wernert P., *Investigation of the unsteady flow velocity field above an airfoil pitching under deep dynamic stall conditions*, Experiments in Fluids, Vol. 19, pp103-111, 1995

[10] Wernert P., Koeber G., Wietrich F., Raffel M., Kompenhans J.,"*Demonstration by PIV of the non-reproductibility of the flow field around an airfoil pitching under deep dynamic stall conditions and consequences thereof*", Aerospace Science and Technology, 1997, n°2, pp125-135

[11] Houdeville R., Juillen J. C., Cousteix J., "*Skin friction measurements with hot-element gauges*", Recherche Aerospatiale, 1984-1

[12] Chandrasekhara M. S., Wilder M. C., "*On the competing mechanisms of compressible dynamic stall*", AIAA Journal, Vol. 36, n°3, March 1998, pp 387-393

[13] Geissler W., Haselmeyer H., "*Investigation of dynamic stall onset*", Aerospace Science and Technology, Vol. 10, n°7, October 2006, pp590-600

[14] O'Meara M. M., Mueller T. J., "*Experimental determination of the laminar separation bubble characteristics of an airfoil at low Reynolds numbers*",

AIAA/ASME 4th Fluid mechanics, Plasma dynamics and Lasers Conference, Atlanta(GA), USA, May 12-14 1986

[15] Richez F., Mary I., Gleize V., Basdevant C., *"Near stall simulation of the flow around an airfoil using zonal RANS/LES coupling method"*, 36th AIAA Fluid Dynamics Conference and Exhibit, San Francisco (CA), USA, June 5-6, 2006

[16] Alam M., Sandham N. D., "*Direct numerical simulation of 'short' laminar separation bubbles with turbulent reattachment*", Journal of Fluid Mechanics, vol. 403, pp. 223-250, 2000

[17] Sankar N. L., Tassa Y., "*Reynolds number and compressibility effects on dynamic stall of a NACA0012 airfoil*", AIAA 18th Aerospace sciences meeting, Pasadena(CA), USA, January 14-16, 1980